Contents lists available at ScienceDirect

Materials Today

journal homepage: www.elsevier.com/locate/mattod

# Nano-structured thin-film reversible solid oxide cells (TF-RSOCs) with exceptionally high performance at low temperatures (≤600℃)

Wonjong Yu [a,1,6], Sanghoon Lee [a,6], Ryosuke Shimizu [b,2], Sangwook Joo [a,3], Tuyen Q. Tran [a], Weikang Li [b], Guomin Zhu [b,4], Y. Shirley Meng [b,5], Nguyen Q. Minh [a,*]

[a] *Center for Energy Research, University of California, San Diego, La Jolla, CA 92093, United States*
[b] *Department of Nano Engineering, University of California, San Diego, La Jolla, CA 92093, United States*

ARTICLE INFO

*Keywords:*
All-sputtered thin-film reversible solid oxide cell (TF-RSOC)
Reversible operation
Nano-columnar electrode structure
Lanthanum nickel cobalt perovskite (LNC)-gadolinium doped ceria (GDC) oxygen electrode

ABSTRACT

This study investigates the fabrication, electrochemical performance, and operation of an all-sputtered thin-film reversible solid oxide cell (TF-RSOC). This TF-RSOC incorporates new LNC ($La_{0.97}Ni_{0.5}Co_{0.5}O_{3-\delta}$)-GDC ($Ce_{0.8}Gd_{0.2}O_{2-\delta}$) oxygen electrode with conventional yttria-stabilized zirconia (YSZ) electrolyte, GDC interlayer, and Ni-GDC hydrogen electrode. The LNC-GDC electrode, which contains no Sr, is formed with a nano-columnar and nano-porous structure by co-sputtering LNC oxide and Gd-Ce metal alloy targets. The all-sputtered TF-RSOC with LNC-GDC oxygen electrode has demonstrated extraordinarily high performance in the temperature range of 500–600 °C, e.g., a peak power density of 2.49 W/cm$^2$ at 600℃ with $H_2$-3 % $H_2O$ and air in fuel cell mode and a current density of 1.68 A/cm$^2$ at 600 ℃ and 1.29 V with 50 % $H_2O$–50 % $H_2$ in electrolysis mode. This performance vastly surpasses that of conventionally sintered RSOCs and TF-RSOCs with state-of-the-art oxygen electrodes, such as LSC (lanthanum strontium cobalt perovskite)-GDC. Cell/electrode structural analysis, electrochemical evaluation, and other characterizations have attributed the exceptional performance enhancement at low temperatures to the nano-columnar and nano-porous structure (with enlarged active area and low tortuosity for oxygen gas transport in electrolysis) and Sr-free composition (without Sr segregation which can cause performance to degrade) of the LNC-GDC electrode. This TF-RSOC has also shown stable performance in short-term (about 40 h) operation without structural failure or defects.

## Introduction

The development of grid-scale clean and sustainable energy storage has received much attention recently because of the increasing demand for the adaption of intermittent renewable energy generation, such as electricity from solar and wind sources [1,2]. Existing energy storage systems, e.g., batteries, require high scale-up costs due to economic constraints originating from limited resources and geographical locations [3]. Solid oxide cells (SOCs) have been considered as a future renewable energy storage technology due to their potential cost-effectiveness and unmatched high efficiency in both fuel cell (in this case, the SOC is a solid oxide fuel cell or SOFC) and electrolysis (in this case, the SOC is a solid oxide electrolysis cell or SOEC) modes [4,5]. The reversibly operating SOC is referred to as a reversible solid oxide cell (RSOC). An RSOC can operate efficiently in SOFC mode to generate electricity with various sources such as hydrogen or hydrocarbon-based fuels and in reverse or SOEC mode to produce hydrogen or syngas by splitting $H_2O$ or mixtures of $H_2O$ and $CO_2$ when DC power is applied to

---

* Corresponding author.
*E-mail address:* nminh@ucsd.edu (N.Q. Minh).

[1] Present address: Department of Mechanical Engineering, Kyung Hee University, 1732, Deogyeong-daero, Giheung-gu, Yongin-si, Gyeonggi-do, 17104, Republic of Korea.

[2] Present address: 24M Technologies 130 Brookline St, Cambridge, MA 02139.

[3] Present address: Clean Hydrogen Research Center, POSCO N.EX.T Hub, POSCO Holdings 67, Cheongam-ro, Nam-gu, Pohang-si, Gyeongsangbuk-do, Republic of Korea.

[4] Present address: Department of Materials, University of California, Santa Barbara, Santa Barbara, CA 93106, United States.

[5] Present address: Pritzker School of Molecular Engineering, University of Chicago, Chicago, IL 60637, United States.

[6] These authors equally contributed to the work: Wonjong Yu, Sanghoon Lee.

https://doi.org/10.1016/j.mattod.2025.10.018
Received 31 March 2025; Received in revised form 9 October 2025; Accepted 27 October 2025

Please cite this article as: Wonjong Yu et al., *Materials Today,* https://doi.org/10.1016/j.mattod.2025.10.018

the cell. Thus, an RSOC can operate in electrolysis mode to produce stored chemical energy sources such as hydrogen or syngas using electricity generated, for example, from wind or solar. When electricity is needed, the RSOC can operate in fuel cell mode to generate electricity from stored hydrogen or syngas [6].

The RSOC is a high-temperature (650–850 ℃) reversible fuel cell-electrolyzer system. Although low-temperature (<100 ℃) reversible systems such as those based on alkaline or proton exchange membrane (PEM) cells are already commercialized, the RSOC is still at its prototype/pre-commercial stage but shows advantages in terms of efficiency, operating current density, and material costs [7,8]. In the case of electrolysis mode, commercial alkaline or PEM electrolyzer systems have been reported to reach an energy-conversion efficiency of up to 80 % [9]. On the other hand, the energy-conversion efficiency of SOC electrolyzers (SOECs) could attain nearly 100 % when the system operates at the thermoneutral voltage and recycles by-product heat [10]. In addition, the theoretical thermoneutral voltage of SOEC is 1.29 V for splitting steam, but that of PEM electrolyzer is much higher, 1.47 V, due to the high kinetic energy barrier for splitting liquid water, leading to a lower current density for PEM electrolyzers at a specified operating voltage [11]. Furthermore, because of the relatively high operating temperature, the activation energy of the catalytic reactions of the RSOC is lower than that of low-temperature electrochemical cells, thus enabling the use of low-cost materials (such as non-precious-metal catalysts) and various fuel sources (including hydrocarbons from existing infrastructure) [12]. Despite these advantages, the RSOC needs to achieve higher current density (e.g., $>1$ A/cm$^2$ in electrolysis mode at the thermoneutral voltage) at low operating temperature ($\leq$600 ℃) to ensure its commercial viability.

Thin-film deposition technologies have been shown to be capable of fabricating SOCs with significantly improved performance at reduced temperatures. Various techniques such as atomic layer deposition (ALD), pulsed laser deposition (PLD), and sputtering deposition have been successfully used for producing high-quality electrolyte films with sub-micro scale and SOC cells with improved performance [13–17]. Recently, the development of high-performance electrode structures based on nano-structured perovskite oxides, which were previously inaccessible via traditional thin-film deposition methods, has become feasible by implementing an advanced co-sputtering process [18,19]. This process, simultaneous sputtering of a ceramic oxide target and a metal alloy target, results in the formation of a backbone structure that enables the production of nano-structured high-performing perovskite oxide-based electrodes. The recently reported research [18,19] has demonstrated a significant reduction in polarization resistance in these nano-structured electrodes compared to conventional sintered oxide or metal electrodes. Unlike sintered electrodes with micro grain size, nano-structured thin-film electrodes frequently display divergent electrochemical properties [18,20–22]. This disparity stems from structural variations at the nano-scale grain level. When optimized, these unique characteristics can play a key role in supporting the development of high-performance thin-film RSOCs (TF-RSOCs) operating at low temperatures.

In general, in order to maintain high performance of the TF-RSOC, especially in long-term operation, it is necessary to stabilize the nanostructure of the electrodes and eliminate other factors that can cause cell performance to degrade. One of the such factors is strontium (Sr) segregation in Sr-containing perovskite oxygen electrodes. Sr segregation in RSOCs significantly affects the catalytic activity of oxygen electrodes by forming surface layers that block active sites needed for oxygen reactions. It leads to a decrease in the electrode's ability to reduce or evolve oxygen efficiently, thus impacting the overall performance and durability of the cell. For example, it is well known that during the operation of SOFCs/SOECs/RSOCs with metallic (e.g., ferritic steel) interconnects, rapid degradation of cell performance caused by chromium poisoning of the oxygen electrode has frequently been observed. One possible reason for this observed degradation is a steady release of strontium from the Sr-containing perovskite material of the oxygen electrode and the reaction of Sr with volatile Cr species (from the metallic interconnect) to form Sr-Cr oxides on the electrode surface. It increases electrode polarization, thus reducing performance [23]. Also, from experimental as well as thermodynamic analysis, it has been shown that Sr-containing oxygen electrodes react with yttria-stabilized zirconia (YSZ) electrolyte, forming insulating phases such as $SrZrO_3$ at temperatures as low as 800 ℃ [24]. A barrier layer or interlayer, such as gadolinium doped ceria (GDC), is commonly introduced to prevent detrimental reactions between the oxygen electrode and the electrolyte.

In this work, we have developed and demonstrated exceptionally high performance at low temperatures ($\leq$600 ℃) for an all-sputtered TF-RSOC with nano-structured electrodes fabricated by the advanced co-sputtering process. This all-sputtered TF-RSOC consists of conventional components (conventional YSZ electrolyte, GDC interlayer, and Ni-GDC hydrogen electrode) and a new Sr-free oxygen electrode (made by co-sputtering of $La_{0.97}Ni_{0.5}Co_{0.5}O_{3\text{-}\delta}$ (LNC) perovskite oxide and $Gd_{0.2}Ce_{0.8}$ (GdCe) alloy), referred to as LNC-GDC. The cell also incorporates a conventional GDC interlayer between the electrolyte and the oxygen electrode. This work demonstrates the superior performance of the co-sputtered LNC-GDC electrode, leading to the extraordinarily high performance observed for the thin-film cell in both fuel cell and electrolysis modes. The co-sputtered perovskite electrode also shows enhanced thermomechanical stability, resulting in the improved performance stability of the all-sputtered cell. The remarkably high performance and stability of the LNC-GDC electrode are not only due to its nano-columnar structure but also because of its Sr-free composition. Through the development of high-performance oxygen electrode material and structure, we demonstrated for the first time an all-sputtered TF-RSOC having a remarkably high performance for reversible operation at low temperatures; for example, at 600 °C, a current density of about 1.68 A/cm$^2$ at 1.29 V with 50 % $H_2O$-50 % $H_2$ in electrolysis mode and a peak power density of about 2.49 W/cm$^2$ with $H_2$-3 % $H_2O$ and air in fuel cell mode.

## Results and discussion

The TF-RSOC investigated in this study was based on the configuration of Ni-GDC hydrogen electrode/YSZ electrolyte/GDC interlayer/LNC-GDC oxygen electrode. In order to create a high-performance RSOC, an all-sputter manufacturing process incorporating co-sputtering of ceramic and metal/alloy targets for the electrodes, especially the oxygen electrode, was employed. The co-sputtering step for the electrodes was designed to produce a highly active nano-columnar structure known for its high-performance characteristics [14,21]. Additionally, the conductive electrodes, especially the oxygen electrode, had thicknesses that were carefully optimized to ensure robust in-plane electrical conductivity while maintaining sufficient porosity. Analysis of the as-deposited LNC-GDC surface (Fig. S1a) shows a relatively dense microstructure with ~1 % porosity, as quantified using image processing software ImageJ. In contrast, the cross-sectional view (Fig. 5c) reveals pronounced columnar porosity deeper in the LNC-GDC, where the difference comes from the intrinsic PVD growth behavior: fan-like growing tendency due to adatom shadowing and surface diffusion, which tend to close pores near the film's top surface. To compare its performance directly with a benchmark electrode material under identical nano-columnar morphology, thickness, and interlayer conditions, LSC–GDC was employed. The cell was manufactured on an anodic aluminum oxide (AAO) substrate with a uniform nano-hole array structure to provide a highly ordered nano-columnar electrode structure [25]. The combination of the advanced sputtering process and the AAO substrate enabled us to produce the cell with electrodes having the nanostructure that exhibited excellent performance.

As shown in Fig. 1, the Ni-GDC hydrogen electrode (fabricated by co-sputtering of Ni and Gd/Ce alloy targets) was nano-porous and nano-columnar with a thickness of 1.20 μm grown uniformly on the AAO

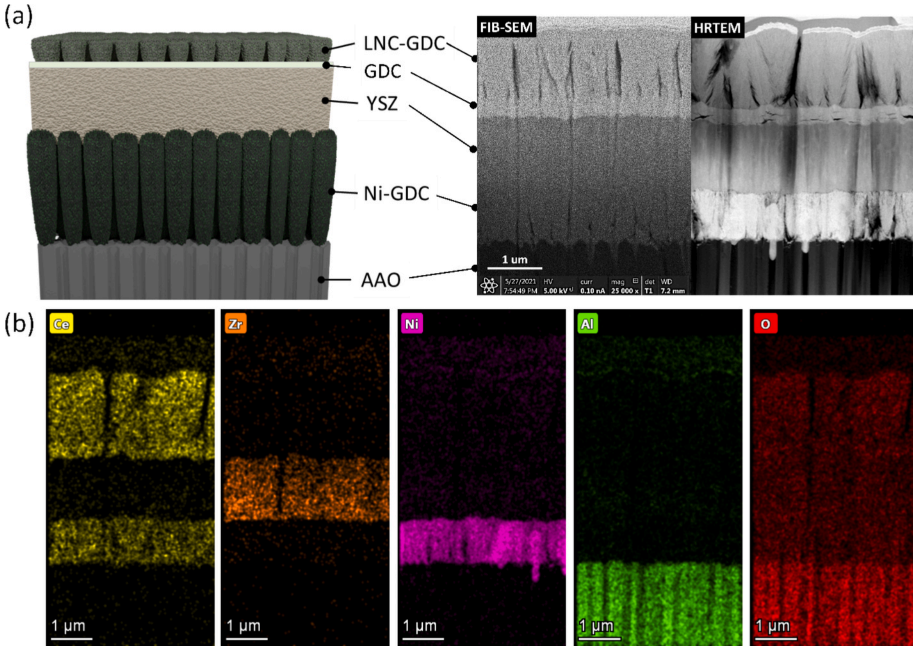

**Fig. 1.** (a) Schematic of all-sputtered TF-RSOC and cross-sectional images of RSOC analyzed by FIB-SEM and HRTEM. (b) EDS-element mapping for the TF-RSOC fabricated on nano-porous substrate.

substrate. The sequentially deposited YSZ electrolyte (about 1.60 μm thick) was produced with a dense structure on top of the hydrogen electrode using a ceramic YSZ target. The low chamber pressure of 0.399 Pa (3 mTorr) was used during sputtering to minimize the number of collisions of sputtered atoms with argon ions, resulting in dense nucleation and growth of YSZ due to the high kinetic energy of sputtered atoms [26]. A GDC interlayer with a fully dense structure was deposited at a thickness of 500 nm on the electrolyte. Considering the lower sinterability of ceria material compared to zirconia-based material, the sputtering for the interlayer used a 0.267 Pa (2 mTorr) of ultra-low chamber pressure [18]. The interlayer was primarily manufactured to activate the interfacial reactions of the oxygen electrode but also to prevent side reactions between YSZ electrolytes and, in the case of, Sr-containing perovskite oxide electrodes [27]. In our previous work, we optimized sputtering power and substrate off-axis displacement to produce fully dense, defect-free GDC films [18], ensuring a reliable diffusion barrier. Numerous studies demonstrate that PVD-deposited GDC layers as thin as 200 nm effectively block Sr migration and prevent insulating phase formation—even at temperatures above 800 ℃ [28,29]. Moreover, interfacial $SrZrO_3$ formation is generally observed only during high-temperature sintering (≥800 ℃) [30,31]. Accordingly, a 500 nm-thick GDC interlayer is more than sufficient to inhibit Sr diffusion at our 550 ℃ operating temperature. Although no elements would cause side reactions in the LNC-GDC oxygen electrode, the same interlayer structure was applied for comparison with conventional $La_{0.6}Sr_{0.4}CoO_{3-\delta}$ (LSC)-GDC.

Finally, the $La_{0.97}Ni_{0.5}Co_{0.5}O_{3-\delta}$ (LNC)-GDC oxygen electrode with a nano-porous and nano-columnar structure (about 1.50 μm thick) was deposited on the interlayer through the advanced co-sputtering process using Gd/Ce metal alloy and LNC oxide targets. Based on the deposition rates for each material, the volumetric ratio of the co-sputtered oxygen electrode materials is approximately 3:7 (LNC or LSC to GDC). Because the LNC perovskite contains 25 at% Ni, the final composite electrode comprises roughly 7.5 at% Ni—significantly lower than the >80 at% Ni in the Ni–GDC hydrogen electrode. This accounts for the stark contrast in Ni signal between the two layers in the EDS maps of Fig. 1(b). The XRD patterns (Fig. S3) of LNC–GDC thin films deposited on Si wafers and YSZ substrates exhibit the characteristic diffraction features of nano-crystalline films, with no secondary or unwanted peaks detected. The focused ion beam (FIB)-scanning electron microscope (SEM) image (Fig. 1(a)) confirms that the all-sputtered TF-RSOC based on AAO substrate with required structural characteristics was successfully fabricated.

In order to evaluate the impacts of the LNC-GDC oxygen electrode on the electrochemical performance of the all-sputtered TF-RSOC, experiments were conducted with symmetrical cells based on the configuration of LNC-GDC/GDC/YSZ/GDC/LNC-GDC to analyze the electrochemical characteristics of the LNC-GDC electrode. Symmetrical cells with conventional oxygen electrodes based on LSC-GDC were also fabricated, and the electrochemical performance of the LSC-GDC electrode was compared with that of the LNC-GDC.

As can be seen in Fig. 2(a), a 200 μm-thick YSZ electrolyte was used as a substrate for symmetrical cells to exclude the effects of other characteristics aside from those electrode structures. GDC interlayers of equal thickness were fabricated by sputtering on both sides of the YSZ electrolyte, and their thickness was controlled uniformly throughout the cell area. The oxygen electrode was deposited by co-sputtering on the GDC interlayers' surface. Deposition conditions were maintained consistently to minimize any possible structural differences between LNC-GDC and LSC-GDC. Therefore, it was assumed through the structural analysis that the differences in electrochemical performance in the symmetrical cell experiments arose from the material property differences between LNC and LSC.

To compare the resistance of oxygen electrode reactions, electrochemical impedance spectroscopy (EIS) analysis was conducted at 600, 650, and 700 ℃ under open-circuit conditions. The results from the symmetrical cell experiments showed that the electrode resistance of the LNC-GDC was over 40 % lower than that of the LSC-GDC (Fig. 2). This trend was consistent throughout the temperature range from 600 ℃ to 700 ℃, with the resistance improvements being more pronounced between 600 ℃ and 650 ℃ than between 650 ℃ and 700 ℃. The LNC-GDC electrode exhibited noteworthy high performance with a polarization resistance of less than 0.005 $\Omega\cdot cm^2$. The following additional analysis identifies the cause of this exceptional performance, as it is not explainable with conventionally sintered material properties.

While LNC demonstrates enhanced polarization resistance when coupled with GDC [32,33], it has been reported that LNC's oxygen ionic conductivity is more than an order of magnitude lower, and its electrical

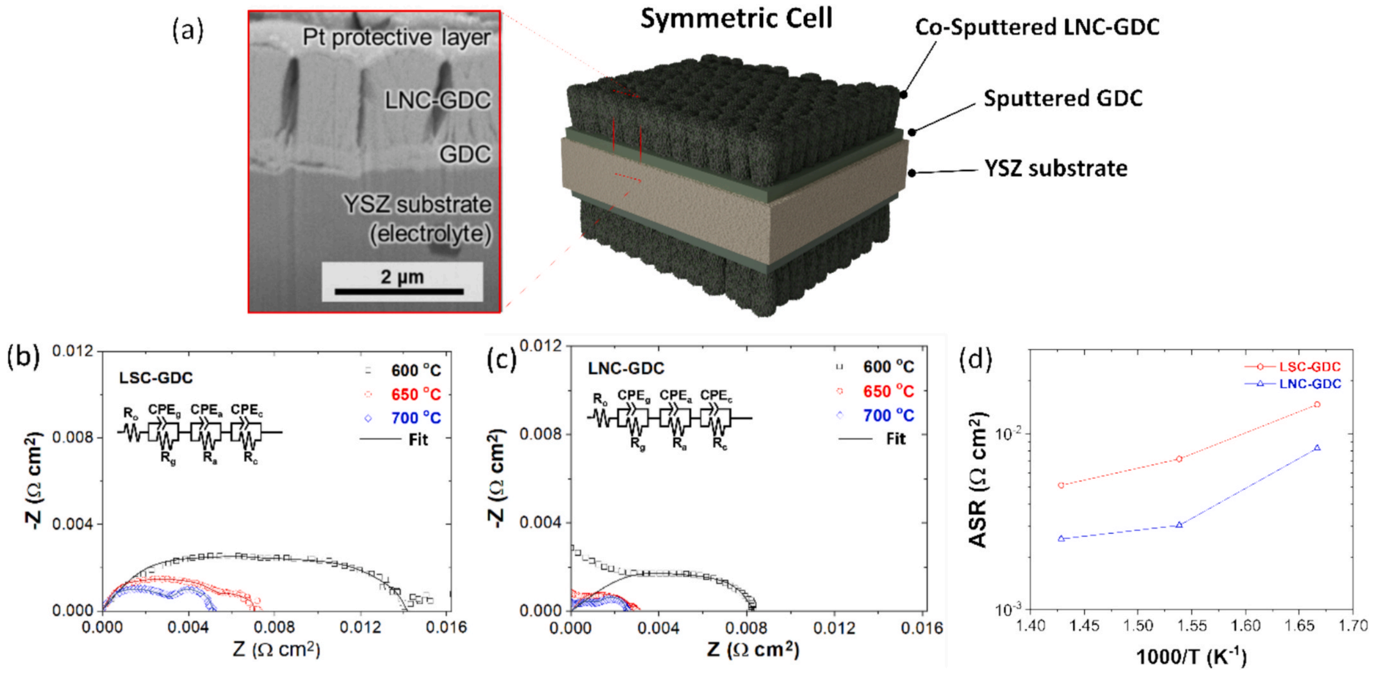

**Fig. 2.** (a) Cross-sectional image of co-sputtered LNC-GDC and GDC interlayer fabricated on YSZ substrate and schematic illustration of the symmetrical cell consisting of the same LNC-GDC electrode on both sides. Electrochemical impedance spectroscopy measurement at OCV for (b) LSC-GDC and (c) LNC-GDC symmetrical cells at 600, 650, 700 °C. (d) Area specific resistances of oxygen electrodes at 600, 650, 700 °C.

conductivity is also slightly lower than those of LSC in the 700–900 °C range [34]. Especially when compared to the state-of-the-art lanthanum strontium cobalt iron perovskite (LSCF) oxygen electrode, LNC also has lower catalytic activity [35]. From this perspective, it can be speculated that the nano-structured LNC-GDC electrode exhibits electrochemical characteristics that differ from those of conventionally sintered perovskite electrodes.

One possibility for such discrepancy in electrochemical properties is the maximization of the Sr segregation effect occurring in the nano-sized Sr-containing electrode. Typically, Sr segregation requires a high operating temperature to happen rapidly. In this study, the symmetrical cells' operating temperature was limited to 700 °C or less. Questions arose as to whether performance degradation of the Sr-containing oxygen electrode could occur at this intermediate operating temperature due to Sr segregation.

To answer this question, surface chemical composition analysis was performed using X-ray photoelectron spectroscopy (XPS) on the sputtered LNC and LSC oxygen electrode samples before and after annealing at 650 °C for 50 h. Fig. 3 shows XPS spectra obtained from LSC and LNC surfaces. La 3d, Sr 3d, and Co 2p spectra from LSC are displayed in Fig. 3 (a)-(c), while Ni 2p, La 3d, Sr 3d, and Co 2p spectra from LNC are displayed in Fig. 3 (d)-(f), respectively. Details of peak fitting and interpretation of each are described below.

Sr 3d spectra can be deconvoluted into two types of sources—surface and lattice—and each has two peaks due to doublet separation. It is assumed that exposure of strontium to air and moisture can form compounds, such as $SrCO_3$ (132.7 eV), SrO (132–135 eV), and $Sr(OH)_2$ (132.8 eV), on the surface [36]. We defined those peaks as "LSC surface" peaks since the binding energies of those peaks are close to each other and are challenging to deconvolute. As-deposited LSC lattice spectra can be regarded as bulk La-Sr-Co-O material. Comparing the as-deposited LSC with the annealed LSC showed that the ratio of surface spectra to lattice increased from 1.01 to 1.40, meaning that $Sr^{2+}$ ions migrated from bulk to surface, reacted with air and/or moisture, and formed carbonate, oxide, and hydroxide Sr by-products. While XPS is an indirect probe of surface composition, multiple angle- and depth-resolved studies have demonstrated Sr enrichment on perovskite cathodes after treatments at as low as 600 °C [37,38], which is in good agreement with our work. The observed XPS results indicate segregation as the primary degradation mode for the Sr-containing oxygen electrodes.

Unlike LSC, the metal components in LNC, i.e., La, Ni, and Co, showed no change in their XPS spectra after the heat treatment, as seen in Fig. 3 (d)-(f). This indicates that LNC had no ion migration from the bulk to the surface, which led to its high-temperature compositional stability. Therefore, the difference in polarization resistance observed in the symmetrical cell tests for LSC and LNC can be attributed to the changes in local chemical composition.

The electrochemical properties and chemical stability of LNC-GDC discussed above confirm the fundamental applicability of this material mixture as an oxygen electrode for the TF-RSOC. Performance of all-sputtered cells formed on AAO substrate in both fuel cell and electrolysis modes were characterized in the temperature range of 500–600 °C to evaluate the reversibility of the LNC-GDC oxygen electrode. The performance of LNC-GDC as an oxygen electrode in complete TF-RSOC cells was compared with that of cells with a LSC-GDC electrode. The deposition conditions were applied identically in both all-sputtered cells to minimize performance differences caused by structural variations. The oxygen electrode was fabricated at a thickness of 1.5 μm. As indicated earlier, except for the oxygen electrodes, all the other cell components were maintained in Ni-GDC/YSZ/GDC configuration on AAO substrates. The co-sputtered Ni-GDC, YSZ, and GDC interlayer were sequentially deposited at 1.20 μm, 1.60 μm, and 500 nm thicknesses, respectively.

Figs. 4(a) and 4(c) show that the all-sputtered TF-RSOC with co-sputtered LSC-GDC oxygen electrode demonstrated high performance, showing peak power density of more than 1.57 W/cm$^2$ at 600 °C with $H_2$-3 % $H_2O$ in fuel cell mode and about 0.700 A/cm$^2$ at 600 °C and thermoneutral voltage of 1.297 V with 50 % $H_2O$-50 % $H_2$ fuel supply in electrolysis mode. Such high performance at low temperatures was attributed to the ultra-thin electrolyte structure and the electrode nanostructure. More interestingly, all-sputtered RSOCs with co-sputtered LNC-GDC electrodes showed remarkably higher performance than the LSC-GDC electrode. The RSOC with LNC-GDC achieved peak power density of 2.49 W/cm$^2$ at 600 °C in fuel cell mode and about 1.68 A/cm$^2$

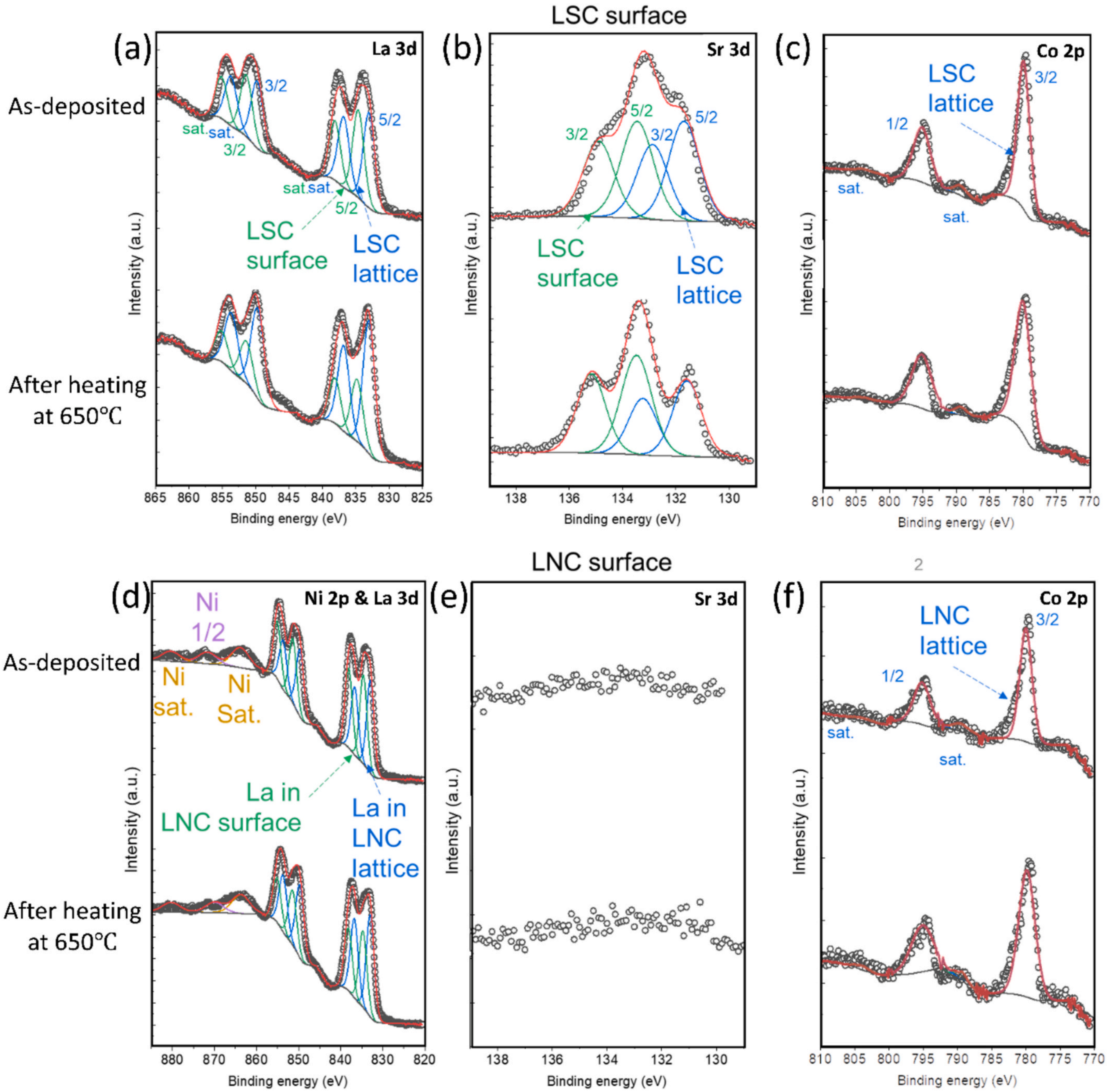

**Fig. 3.** XPS spectra of LSC as deposited and after annealing at 650 ℃ for 50 h for (a) La 3d, (b) Sr 3d, and (c) Co 2p. XPS spectra of LNC as deposited and after annealing at 650 ℃ for 50 h for (d) Ni 2p and La 3d, (e) Sr 3d (binding energy from 130-138 eV) and (f) Co 2p.

at 600 ℃ and thermoneutral voltage of 1.28 V in electrolysis mode, under the same respective fuel conditions (Fig. 4 (b) and 4(d)). From the LSC-GDC cell to the LNC-GDC cell, the peak power density in fuel cell mode increased by 67 %, and the electrolysis current density at the thermoneutral voltage leaped by 113 %. This exceptionally high performance of the LNC-GDC cell was consistent with the polarization resistances obtained from the symmetrical cell tests. Figs. S4 and S5 and Tables S1 and S2 in the Supporting Information compare our cell's performance at 500-600 ℃ with literature values, showing that it matches or exceeds the fuel cell and electrolysis performance of recently reported high-performance materials.

The performance difference between the two all-sputtered cells was attributed to the catalytic property differences between LNC and LSC since the thickness and nano-structure of the electrolyte and the hydrogen electrode were identically fabricated. Detailed analysis of these performance differences was conducted through electrochemical impedance spectroscopy (EIS) at 0.7 V and 500, 550, and 600 ℃ and shown on Fig. 4 (e). The apparent offset of the Nyquist curves at high frequencies on the imaginary axis is not a true electrochemical response but rather a parasitic inductive artifact from the measurement loop—primarily the cell holder, wiring, and current collectors. This residual inductance causes the high-frequency intercept to shift above zero on the imaginary axis.

While the conventional LSC-GDC cell showed a polarization resistance of 0.095 Ω·cm$^2$ at 600 ℃, still considerably lower than reported literature values for LSC-GDC cathode, the LNC-GDC cell measured even lower with an area-specific resistance (ASR) of 0.031 Ω·cm$^2$. Notably, the LNC-GDC cell exhibited overall lower ohmic resistance, measuring

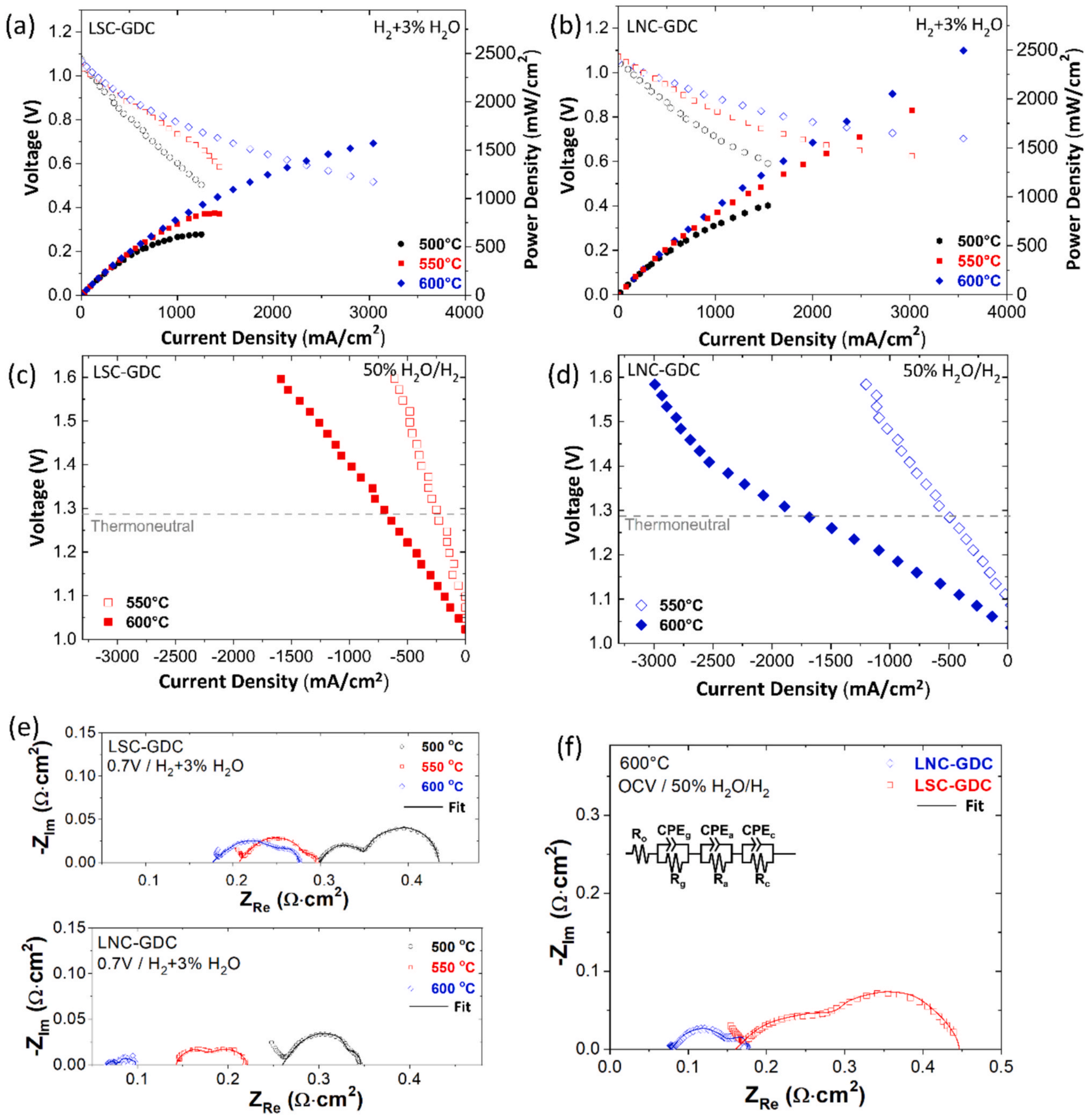

**Fig. 4.** Electrochemical performance of all-sputtered TF-RSOCs with LSC–GDC and LNC–GDC oxygen electrodes: (a, b) Current density–voltage–power (i–V–P) curves at 500 °C, 550 °C, and 600 °C; (c, d) Electrolysis current density–voltage behavior at 550 °C and 600 °C; (e, f) Nyquist plots under (e) 0.7 V and (f) open-circuit conditions. Solid lines in (e) and (f) are fits to the equivalent-circuit model shown in (f).

0.259, 0.145, and 0.067 Ω·cm$^2$ at 500 °C, 550 °C, and 600 °C, respectively, compared to the LSC-GDC cell, which had ohmic resistances of 0.299, 0.212, and 0.181 Ω·cm$^2$.

Contrary to the reportedly lower conductivity of conventionally prepared LNC compared to LSC in the 500-600 ℃ range, LNC with the same nano-structure performed better than LSC on the all-sputtered TF-RSOC platform. Analysis of the surface composition by XPS presented in Fig. 3 revealed an increased surface Sr composition ratio for LSC annealed at 650 ℃. It led to the inference that Sr segregation lowers LSC's conductivity and surface reactivity. Since LNC is Sr-free, no performance degradation due to segregation occurred, leading to higher electrode performance. Generally, no abrupt degradation due to segregation has been reported at temperatures below 700 ℃ in short times (< 50 h). However, in the case of the co-sputtered LSC-based electrode with nano-sized particles and a columnar structure, surface composition changes could occur more rapidly, as nano-sized grains exhibit exponentially higher reactivity due to several orders higher surface-to-volume ratio than sintered structures [39]. Because limited adatom mobility and atomic shadowing under low substrate temperatures and moderate pressures impede grain coalescence during deposition [40], porous columnar nanostructures produced by magnetron sputtering inherently exhibit very high surface-to-volume ratios—often several orders of magnitude greater than conventionally sintered powders. XPS analysis validated this inference by confirming significant changes in the Sr surface ratio even in a relatively short time and low-temperature conditions.

The superior performance of the LNC-GDC cell in the electrolysis mode, confirmed via EIS measurements at open-circuit voltage (OCV) under the 50 % $H_2O$-50 % $H_2$ conditions at 600 ℃ (Fig. 4 (f)), indicated improvements in both ohmic and polarization resistances compared to the LSC-GDC cell. The material characteristics of LNC brought these enhancements. In addition, the nano-columnar structure of the oxygen electrode (with a column width of less than 1 μm) fabricated by co-sputtering may exhibit significant advantages during the electrolysis process.

The superior performance of the nanostructured LNC-GDC is yet to be explored theoretically. Direct theoretical modeling (e.g., DFT-based comparison of oxygen vacancy formation energies, B-site redox energetics, and surface adsorption thermodynamics) between LNC and conventional Sr-doped perovskites like LSC remains largely unexplored in the literature. This gap is due in part to the complexity of modeling multi-component oxides such as $LaNi_{1-x}Co_xO_{3-\delta}$, especially in the presence of nanostructured architectures and potential local ordering phenomena at the B-site. Furthermore, prior DFT efforts have primarily focused on simpler Co–Fe or Co-only systems, which limits their direct applicability to LNC compositions.

One of the leading causes of degradation in SOECs is delamination or crack formation of the oxygen electrode due to oxygen evolution at the interface during electrolysis [41]. The high tortuosity of the conventional sintered electrode structure can lead to trapped oxygen gas, resulting in pressure buildup, which can physically damage the bond between the electrode and electrolyte. The nano-columnar structure could mitigate such SOEC degradation. Since the columnar structure has a tortuosity of nearly 1, there is a high probability that oxygen gas trapping will not occur.

As seen in Fig. 5(a), even with alternating cyclic operation at 1.3 V (electrolysis mode) and 0.75 V (fuel cell mode) at 550 ℃, the cell maintained high performance exceeding 1 A/$cm^2$ in the electrolysis mode. The initial rise in current density during the first 10 h reflects *in situ* activation of both electrodes. Upon reaching 550 °C, the room-temperature–deposited LNC–GDC layer undergoes grain growth and improved crystallographic ordering, transiently enhancing catalytic activity and lowering polarization resistance. At the same time, surface NiO on the Ni–GDC fuel electrode is reduced under hydrogen, improving Ni/GDC connectivity and TPB coverage, while thermal equilibration of the YSZ and GDC films boosts oxygen-ion conductivity. Because AAO-supported thin-film cells omit a separate Ni–YSZ pre-reduction, these activation processes occur during normal operation rather than in a lengthy pre-treatment. After this activation phase, the current gradually returns to its baseline. In electrolysis mode under low humidity, Ni wettability on GDC worsens (contact angles increase), reducing TPB coverage [42]. Evolving gas compositions and slight relaxation at the electrode/electrolyte interface also contribute to this decay, with no signs of permanent microstructural degradation.

It also showed stable performance for 40 h in fuel cell mode at 0.75 V (Fig. 5(b)). This 40 h of operation has been the most extended operation reported in the field of all-sputtered SOC research [19,43]. The nanostructure after such an operation was examined through the FIB-SEM cross-section. Fig. 5(d) shows that no noticeable structural deformation occurred after the operation. Notably, the oxygen electrode retained its columnar structure, and there was no electrode delamination, indicating that no structural failure occurred due to the oxygen evolution reaction during the electrolysis operation. Grain size distribution of as-deposited LNC-GDC electrode and surface FESEM images before and after the 40 h of operation are shown in Supporting Information (Fig. S1 and S2).

Potential long-term degradation mechanisms include nanocolumn coarsening and interfacial delamination. Magnetron-sputtered thin films

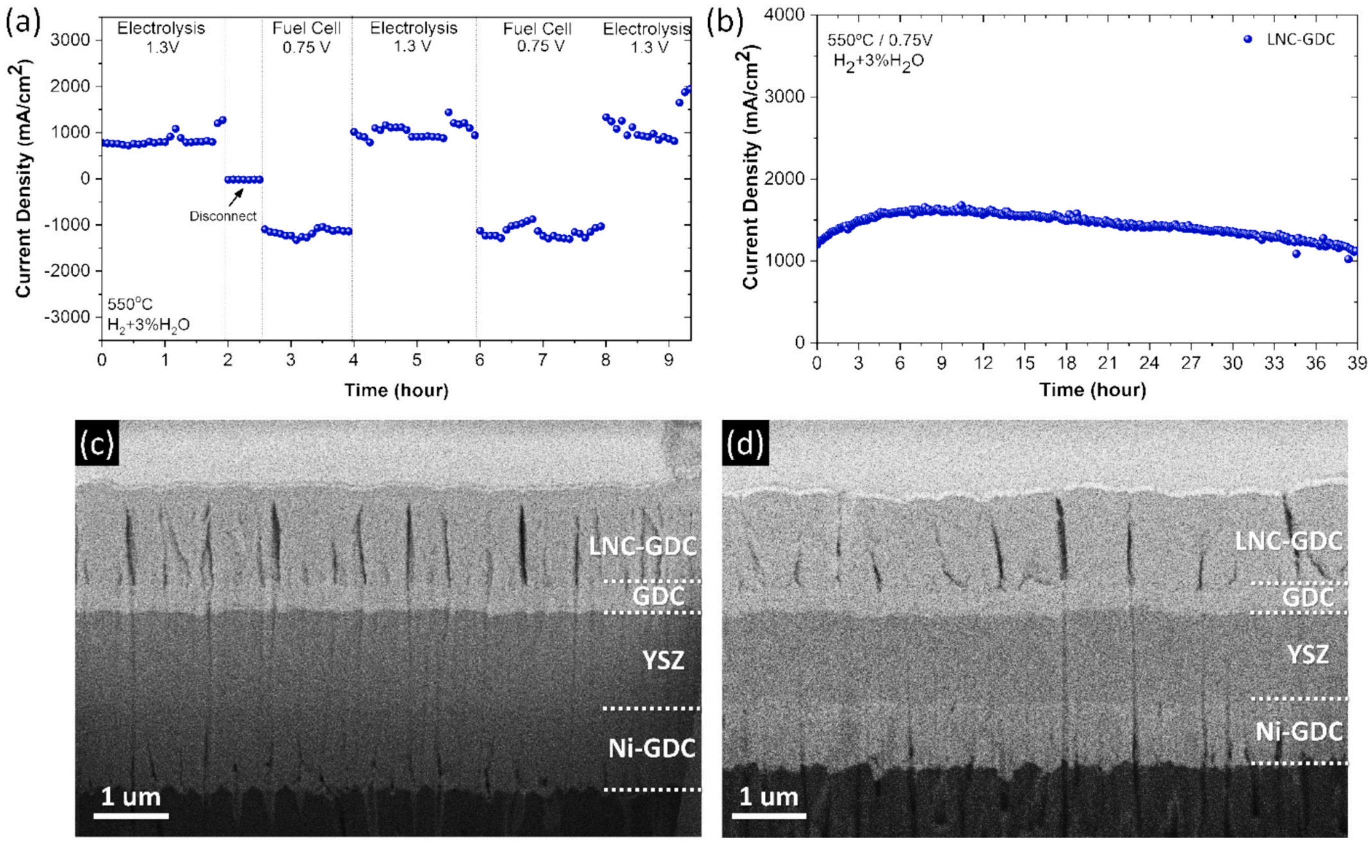

**Fig. 5.** (a) Cycling operation of the all-sputtered RSOC at 0.75 V (fuel cell mode) and 1.3 V (electrolysis mode) at 550 °C. (b) Constant-voltage fuel-cell operation at 0.75 V and 550 °C. (c, d) Cross-sectional micrographs of the LNC–GDC cell before and after the operation in (b), acquired at detector tilt angles of 48° (c) and 52° (d). The apparent layers′ thickness difference is a tilt artifact; both samples share the same nominal component thickness.

carry intrinsic compressive stress, which can exacerbate defect formation over time. In addition, the highly porous, nano-columnar electrode is prone to thermally activated grain growth—driven by surface and grain-boundary diffusion (often termed thermal coarsening)—to reduce its surface energy, losing its physical properties. Introducing an *in situ* or post-deposition anneal can stabilize the grain structure, thereby enhancing durability.

## Conclusion

In summary, the all-sputtered TF-RSOC cells of the configuration Ni-GDC/YSZ/GDC/LNC-GDC with required structural and other characteristics were successfully fabricated in this study. The LNC-GDC oxygen electrode produced by co-sputtering of LNC oxide and Gd-Ce alloy targets was nano-porous with a nano-columnar structure. This electrode showed lower polarization resistance than conventional LSC-GDC electrodes fabricated and tested under identical conditions. The all-sputtered RSOC incorporating the LNC-GDC oxygen electrode demonstrated exceptionally high performance in both fuel cell and electrolysis modes at low temperatures (500-600 ℃), e.g., at 600 °C, a peak power density of about 2.49 W/cm$^2$ with $H_2$-3 % $H_2O$ and air in fuel cell mode and a current density of about 1.68 A/cm$^2$ at 1.28 V and 50 % $H_2O$-50 % $H_2$ in electrolysis mode. This performance dramatically exceeds that of conventional RSOCs and even TF-RSOCs with conventional LSC-GDC oxygen electrodes. Such high performance is attributed to the nano-columnar structure, as well as the Sr-free chemical composition of the LNC-GDC. The nano-columnar structure with low tortuosity enlarges the electrode's active area and facilitates oxygen gas transport in electrolysis operation. The Sr-free composition eliminates the Sr segregation, which can cause oxygen electrode degradation. The all-sputtered TF-RSOC maintained stable and high performance during cyclic operation between fuel cell and electrolysis modes. The cell exhibited performance exceeding 1.20 A/cm$^2$ for nearly 40 h at a constant voltage of 0.75 V operation at 550 ℃ with no observed structural defects. This study demonstrates the fabrication, especially the fabrication of LNC-GDC oxygen electrodes with nano-columnar structure by co-sputtering, exceptionally high performance, and stable operation in short-term cyclic testing for the all-sputtered TF-RSOC.

## Experimental section

### *Fabrication of all-sputtered thin-film reversible solid oxide cells (TF-RSOCs)*

For the fabrication of all-sputtered TF-RSOC cells, an anodic aluminum oxide (AAO) (InRedox, USA), characterized by an average pore diameter of 160 nm, was employed as the supporting substrate. This substrate (1 × 1 cm$^2$ size, 100 μm thick) possessed highly uniform and parallel nano-pores, self-organizing into a honeycomb shape. The substrate was thoroughly cleaned with ethanol and acetone in sonication for 30 min to eradicate any surface contamination.

The Ni-GDC hydrogen electrode was deposited on the AAO utilizing direct current (DC) magnetron sputtering using an AJA Orion magnetron sputtering system in a single chamber. 3-inch (76 mm) Nickel (Ni) and 2-inch (51 mm) $Gd_{0.2}Ce_{0.8}$ alloy targets (AJA Internationals, USA), both with 99.9 % purity, were employed, with 200 W power for both targets and a chamber pressure of 4 Pa (30 mTorr), controlled by ultra-high purity Ar gas (99.9995 %). The critical factors in forming the desired nanostructure on the honeycomb-like substrate were the substrate rotation speed and the deposition angle, which were fixed at 6.0 rpm and 75°, respectively.

Yttria-stabilized zirconia (8 mol% YSZ) and gadolinium-doped $CeO_2$ (10 mol% GDC) 3-inch targets (Advanced Energy Materials Limited, China) were used for the fabrication of the electrolyte and interlayer. A 1.6 μm-thick fully dense YSZ electrolyte was deposited on top of the Ni-GDC electrode using a radio frequency (RF) sputtering at conditions of 200 W and 0.400 Pa (3 mTorr), with the chamber pressure regulated by Ar flow. Sequentially, a 500 nm-thick defect-free and fully dense GDC was fabricated at 0.267 Pa (2 mTorr) and 150 W. A substrate rotation speed of 2.0 rpm and a deposition angle of 90° were maintained during the deposition of YSZ and GDC.

For the LNC-GDC and LSC-GDC oxygen electrodes, $La_{0.97}Ni_{0.5}Co_{0.5}O_{3-\delta}$ (LNC) and $La_{0.6}Sr_{0.4}CoO_{3-\delta}$ (LSC) 2-inch targets (99.9 %, Advanced Energy Materials Limited, China) were used with 150 W RF sputtering, in conjunction with a 3-inch diameter Gd-Ce alloys (20:80 at %) target (AJA Internationals, USA) at 30 W DC sputtering and 4 Pa chamber pressure. The substrate was rotated at 6.0 rpm, and a deposition angle of 45° was used for the 2-inch target, while a normal deposition angle was employed for the 3-inch Gd-Ce alloy target. The thickness for the oxygen electrode was uniformly controlled to 1.20 μm, and the active area of the cathode was shaped by employing a physical patterned mask. The volumetric ratio of the co-sputtered oxygen electrode materials were decided based on the deposition rates for each material (~3 nm/min for LNC target and ~7 nm/min for Gd/Ce target), which was approximately 3:7 (LNC or LSC to GDC). For the samples characterized electrochemically, a 150-nm-thick Pt current collection layer was deposited atop the oxygen electrode using a 2-inch diameter Pt target (AJA International, USA) under the same deposition conditions as those for the oxygen electrode. The LNC-GDC and LSC-GDC symmetrical cells were fabricated under the same deposition conditions as the AAO-based TF-RSOCs, with the GDC interlayer and the LSC-GDC and LNC-GDC oxygen electrodes deposited on both sides of the YSZ substrates (FuelCell Materials, USA).

### *Sputtered film characterization*

Field emission scanning electron microscopy (FESEM) (Apreo SEM, FEI Company, USA), with less than 5 nm-thick platinum coating on each sample, was used to examine the surface and cross-section nano-structure. In addition, the sample cross-sectional nano-structure was examined by a focused ion beam (FIB) (3D FEG, FEI Company, USA). High-resolution transmission electron microscopes (HR-TEM) (JEM-2100F, JEOL Ltd., Japan) equipped with energy-dispersive X-ray spectroscopy (EDS) were used for detailed structural analysis, and grain size investigation. The crystal structure of the sputtered oxygen electrode was characterized by an X-ray diffractometer (XRD) (X'pert Pro, PANalytical, the Netherlands) with Cu Kα. To evaluate Sr segregation in each material, the sputtered LNC and LSC samples were annealed at 650 ℃ for 50 h. The chemical composition of the LNC and LSC oxygen electrode surfaces with and without annealing was determined through X-ray photoelectron spectroscopy (XPS) (AXIS-His, Kratos, Japan) with a binding energy range between 0 and 1000 eV, employing a 3 × 3 mm$^2$ X-ray spot.

### *Electrochemical characterization*

All-sputtered TF-RSOC cells based on the AAO substrate were attached to an alumina holder using a carefully selected combination of silver paste and ceramic sealant. Our group's previous publications describe the electrochemical test setup and protocol details [18,19]. Thermal regulation was achieved with a custom-built furnace that allowed for stringent control over the cell's temperature, and the tests were conducted at 500, 550, and 600 ℃. For fuel cell mode experiments, the hydrogen electrode environment was maintained by a constant flow of 25 sccm hydrogen gas through a distilled water bubbler at room temperature, while the oxygen electrode was exposed to a controlled ambient air atmosphere. For electrolysis mode experiments, steam was generated by bubbling hydrogen through water heated to 81.4 ℃, while the oxygen electrode was also exposed to ambient air.

The electrochemical evaluation was conducted by employing Gamry Reference 3000 potentiostat (Gamry Instruments, Inc,. USA). The current density–voltage (i–V) curves were obtained by scanning from open-circuit voltage (OCV) to 0.5 V for fuel cell mode and to 1.6 V for electrolysis mode at a scan rate of 25 mV/s. For the LNC-GDC cells, the measurement was terminated before reaching 0.5 V to prevent electrode damage due to joule heating from excessive current. A detailed electrochemical impedance spectroscopy (EIS) analysis was conducted at 0.7 V and OCV conditions across a broad frequency range from 1 MHz to 2 Hz, with a carefully calibrated signal amplitude of 30 mV. Symmetrical cell test of the oxygen electrode materials prepared on the YSZ substrates was conducted at 600, 650, and 700 ℃ under ambient air environment. EIS analysis was carried out for the symmetrical cells under OCV conditions at each temperature.

## CRediT authorship contribution statement

**Wonjong Yu:** Writing – original draft, Methodology, Investigation, Formal analysis, Data curation, Conceptualization. **Sanghoon Lee:** Writing – review & editing, Writing – original draft, Visualization, Validation, Investigation, Formal analysis. **Ryosuke Shimizu:** Investigation, Formal analysis. **Sangwook Joo:** Methodology, Conceptualization. **Tuyen Q. Tran:** Validation. **Weikang Li:** Formal analysis. **Guomin Zhu:** Formal analysis. **Y. Shirley Meng:** Resources, Funding acquisition. **Nguyen Q. Minh:** Writing – review & editing, Supervision, Resources, Project administration, Funding acquisition.

## Declaration of competing interest

The authors declare that they have no known competing financial interests or personal relationships that could have appeared to influence the work reported in this paper.

## Acknowledgments

This work is funded by the U.S. Department of Energy/National Energy Technology Laboratory (DOE/NETL) under Cooperative Agreement DE-FE0031940.

## Appendix A. Supplementary data

Supplementary data to this article can be found online at https://doi.org/10.1016/j.mattod.2025.10.018.

## Data availability

Data will be made available on request.

## References

[1] A. Hauch, et al., Recent advances in solid oxide cell technology for electrolysis, Science 370 (2020) eaba6118, https://doi.org/10.1126/science.aba6118.

[2] M.B. Mogensen, et al., Reversible solid-oxide cells for clean and sustainable energy, Clean Energy 3 (2019) 175–201, https://doi.org/10.1093/ce/zkz023.

[3] H. Lund, et al., Energy storage and smart energy systems, Int. J. Sustain. Energy Plan. Manage. 11 (2016) 3–14, https://doi.org/10.5278/ijsepm.2016.11.2.

[4] K. Eguchi, T. Hatagishi, H. Arai, Power generation and steam electrolysis characteristics of an electrochemical cell with a zirconia- or ceria-based electrolyte, Solid State Ion. 86–88 (1996) 1245–1249, https://doi.org/10.1016/0167-2738(96)00295-0.

[5] S.Y. Gómez, D. Hotza, Current developments in reversible solid oxide fuel cells, Renew. Sustain. Energy Rev. 61 (2016) 155–174, https://doi.org/10.1016/j.rser.2016.03.005.

[6] N.Q. Minh, M.B. Mogensen, Reversible solid oxide fuel cell technology for green fuel and power production, the, Electrochem. Soc. Interface 22 (2013) 55–62, https://doi.org/10.1149/2.F05134if.

[7] T.D. Hutty, et al., Long term energy storage with reversible solid oxide cells for microgrid applications, Energy Rep. 7 (2021) 24–33, https://doi.org/10.1016/j.egyr.2021.02.059.

[8] M.A. Laguna-Bercero, Recent advances in high temperature electrolysis using solid oxide fuel cells: a review, J. Power Sources 203 (2012) 4–16, https://doi.org/10.1016/j.jpowsour.2011.12.019.

[9] M. Arunachalam, D.S. Han, Efficient solar-powered PEM electrolysis for sustainable hydrogen production: an integrated approach, Emergent Mater. 7 (2024) 1401–1415, https://doi.org/10.1007/s42247-024-00697-y.

[10] Z. Wang, M. Mori, T. Araki, Steam electrolysis performance of intermediate-temperature solid oxide electrolysis cell and efficiency of hydrogen production system at 300 Nm3 h−1, Int. J. Hydrogen Energy 35 (2010) 4451–4458, https://doi.org/10.1016/j.ijhydene.2010.02.058.

[11] K. Onda, et al., Prediction of production power for high-pressure hydrogen by high-pressure water electrolysis, J. Power Sources 132 (2004) 64–70, https://doi.org/10.1016/j.jpowsour.2004.01.046.

[12] N.Q. Minh, Ceramic fuel cells, J. Am. Ceram. Soc. 76 (1993) 563–588, https://doi.org/10.1111/j.1151-2916.1993.tb03645.x.

[13] J.H. Shim, et al., Atomic layer deposition of yttria-stabilized zirconia for solid oxide fuel cells, Chem. Mater. 19 (2007) 3850–3854, https://doi.org/10.1021/cm070913t.

[14] S. Lee, et al., A nanoporous substrate-based low temperature solid oxide fuel cell using a thin film Ni anode, Thin Solid Films 666 (2018) 177–181, https://doi.org/10.1016/j.tsf.2018.09.039.

[15] S. Lee, et al., Effect of plasma-enhanced atomic layer deposited YSZ inter-layer on cathode interface of GDC electrolyte in thin film solid oxide fuel cells, Renew. Energy 144 (2019) 123–128, https://doi.org/10.1016/j.renene.2018.11.021.

[16] J.H. Park, et al., A nanoarchitectured cermet composite with extremely low Ni content for stable high-performance solid oxide fuel cells, Acta Mater. 206 (2021), https://doi.org/10.1016/j.actamat.2020.116580.

[17] I. Chang, et al., Ultrathin YSZ coating on Pt cathode for high thermal stability and enhanced oxygen reduction reaction activity, Adv. Energy Mater. 5 (2015), https://doi.org/10.1002/aenm.201402251.

[18] Y.H. Lee, et al., All-sputtered, superior power density thin-film solid oxide fuel cells with a novel nanofibrous ceramic cathode, Nano Lett. 20 (2020) 2943–2949, https://doi.org/10.1021/acs.nanolett.9b02344.

[19] H. Ren, et al., Nano-ceramic cathodes via co-sputtering of Gd–Ce alloy and lanthanum strontium cobaltite for low-temperature thin-film solid oxide fuel cells, ACS Appl. Energy Mater. 3 (2020) 8135–8142, https://doi.org/10.1021/acsaem.0c01147.

[20] W. Yu, et al., Enhanced performance of nanostructured thin film anode through Pt plasma enhanced atomic layer deposition for low temperature solid oxide fuel cells, Int. J. Hydrogen Energy 45 (2020) 32816–32824, https://doi.org/10.1016/j.ijhydene.2020.03.158.

[21] W. Yu, et al., High performance, enhanced structural stability of co-sputtered nanocomposite anode with neutral stress state for low-temperature solid oxide fuel cells, Mater. Today Energy 34 (2023), https://doi.org/10.1016/j.mtener.2023.101308.

[22] H.-S. Noh, et al., The potential and challenges of thin-film electrolyte and nanostructured electrode for yttria-stabilized zirconia-base anode-supported solid oxide fuel cells, J. Power Sources 247 (2014) 105–111, https://doi.org/10.1016/j.jpowsour.2013.08.072.

[23] L. Niewolak, F. Tietz, W.J. Quadakkers, Interconnects, in: high-temperature solid oxide fuel cells for the 21st century, 2016, pp. 195–254.

[24] S.P. Jiang, Development of lanthanum strontium cobalt ferrite perovskite electrodes of solid oxide fuel cells – a review, Int. J. Hydrogen Energy 44 (2019) 7448–7493, https://doi.org/10.1016/j.ijhydene.2019.01.212.

[25] J. Park, et al., Engineering of the electrode structure of thin film solid oxide fuel cells, Thin Solid Films 584 (2015) 125–129, https://doi.org/10.1016/j.tsf.2014.11.018.

[26] K. Meyer, I.K. Schuller, C.M. Falco, Thermalization of sputtered atoms, J. Appl. Phys. 52 (1981) 5803–5805, https://doi.org/10.1063/1.329473.

[27] R. Knibbe, et al., Cathode–electrolyte interfaces with CGO barrier layers in SOFC, J. Am. Ceram. Soc. 93 (2010) 2877–2883, https://doi.org/10.1111/j.1551-2916.2010.03763.x.

[28] H.S. Ur Rehman, N. Coppola, A. Singh, P. Polverino, G. Carapella, D. Montinaro, F. Martinelli, B. Morel, J. Mougin, A. Galdi, C. Pianese, L. Maritato, Gadolinium-doped ceria room-temperature sputtered thin barrier layers in large-area solid oxide fuel cells: influence of their thickness and thickness gradient on the cathodic processes, ACS Appl. Energy Mater., 8 (2025) 4281–4287. https://doi.org/10.1021/acsaem.4c03180.

[29] P. Coddet, et al., Characteristics and properties of a magnetron sputtered gadolinia-doped ceria barrier layer for solid oxide electrochemical cells, Surf. Coat. Technol. 339 (2018) 57–64, https://doi.org/10.1016/j.surfcoat.2018.01.079.

[30] K. Yang, et al., Formation of La2Zr2O7 or SrZrO3 on cathode-supported solid oxide fuel cells, J. Power Sources 159 (2006) 63–67, https://doi.org/10.1016/j.jpowsour.2006.04.049.

[31] K. Chen, et al., Direct application of cobaltite-based perovskite cathodes on the yttria-stabilized zirconia electrolyte for intermediate temperature solid oxide fuel cells, J. Mater. Chem. A 4 (2016) 17678–17685, https://doi.org/10.1039/c6ta07067a.

[32] S. Ovtar, et al., Comparison between La0.6Sr0.4CoO3-d and LaNi0.6Co0.4O3-d infiltrated oxygen electrodes for long-term durable solid oxide fuel cells, Electrochim. Acta 266 (2018) 293–304, https://doi.org/10.1016/j.electacta.2018.02.022.

[33] N. Duan, et al., Multi-functionalities enabled fivefold applications of LaCo0.6Ni0.4O3−δ in intermediate temperature symmetrical solid oxide fuel/electrolysis cells, Nano Energy 77 (2020), https://doi.org/10.1016/j.nanoen.2020.105207.

[34] P. Hjalmarsson, et al., Structural properties and electrochemical performance of strontium- and nickel-substituted lanthanum cobaltite, Solid State Ion. 179 (2008) 636–646, https://doi.org/10.1016/j.ssi.2008.04.026.

[35] Q. Ma, et al., Characterization and optimization of La0.97Ni0.5Co0.5O3−δ-based air-electrodes for solid oxide cells, ACS Appl. Energy Mater. 1 (2018) 2784–2792, https://doi.org/10.1021/acsaem.8b00456.

[36] Z. Cai, et al., Chemical heterogeneities on La0.6Sr0.4CoO3−δ thin films—correlations to cathode surface activity and stability, Chem. Mater. 24 (2012) 1116–1127, https://doi.org/10.1021/cm203501u.

[37] E. Mutoro, et al., Reversible compositional control of oxide surfaces by electrochemical potentials, J. Phys. Chem. Lett. 3 (2011) 40–44, https://doi.org/10.1021/jz201523y.

[38] W. Jung, H.L. Tuller, Investigation of surface Sr segregation in model thin film solid oxidefuel cell perovskite electrodes, Energy Environ. Sci. 5 (2012) 5370–5378, https://doi.org/10.1039/c1ee02762j.

[39] A. Zaluska, L. Zaluski, J.O. Ström-Olsen, Structure, catalysis and atomic reactions on the nano-scale: a systematic approach to metal hydrides for hydrogen storage, Appl. Phys. A Mater. Sci. Process. 72 (2001) 157–165, https://doi.org/10.1007/s003390100783.

[40] J.A. Thornton, High rate thick film growth, Annu. Rev. Mater. Sci. 7 (1977) 239–260, https://doi.org/10.1146/annurev.ms.07.080177.001323.

[41] K.F. Chen, S.P. Jiang, Failure mechanism of (La,Sr)MnO3 oxygen electrodes of solid oxide electrolysis cells, Int. J. Hydrogen Energy 36 (2011) 10541–10549, https://doi.org/10.1016/j.ijhydene.2011.05.103.

[42] S. Ihara, et al., Wettability analysis of Ni/YSZ interface under operating conditions of solid oxide cells, J. Power Sources 654 (2025), https://doi.org/10.1016/j.jpowsour.2025.237867.

[43] W. Yu, et al., Low-temperature, high-performance thin-film solid oxide fuel cells with tailored nano-column structures of a sputtered Ni anode, J. Mater. Chem. A 8 (2020) 21668–21679, https://doi.org/10.1039/d0ta06255c.